ADVANCED FUNCTIONAL MATERIALS

Supporting Information

for *Adv. Funct. Mater.,* DOI: 10.1002/adfm.202111556

Significant Increase of Electron Thermal Conductivity in Dirac Semimetal Beryllonitrene by Doping Beyond Van Hove Singularity

Zhen Tong, Alessandro Pecchia, ChiYung Yam, Hua Bao, Traian Dumitrică,* and Thomas Frauenheim**

Supplemental Material:

Significant Increase of Electron Thermal Conductivity in Dirac Semimetal Beryllonitrene by Doping Beyond van Hove Singularity

Zhen Tong,[1,2,*] Alessandro Pecchia,[3] ChiYung Yam,[1,2] Hua Bao,[4] Traian Dumitrică,[5,†] and Thomas Frauenheim[1,2,6,‡]

[1]*Shenzhen JL Computational Science and Applied Research Institute, Shenzhen 518131, China.*

[2]*Beijing Computational Science Research Center, Beijing 100193, China*

[3]*CNR-ISMN, Via Salaria km 29.300, Monterotondo 00017, Rome, Italy*

[4]*University of Michigan-Shanghai Jiao Tong University Joint Institute, Shanghai Jiao Tong University, Shanghai 200240, China.*

[5]*Department of Mechanical Engineering, University of Minnesota, Minnesota 55455, United States of America*

[6]*Bremen Center for Computational Materials Science, University of Bremen, Bremen 2835, Germany*

S1. Methodology

S1.1. Phonon transport

As given in Eq. (1) in the main text, the phonon thermal conductivity tensor ($\kappa_{\rm ph}^{\alpha\beta}$) can be written as a summation over all phonon modes $\lambda = (\mathbf{q}, \nu)$ of polarization ν, wave vector $\mathbf{q}$ and frequency ω_λ [1–4] by solving the Boltzmann transport equation (BTE) combining with Fourier's law of heat conduction [5],

$$\kappa_{\rm ph}^{\alpha\beta} = \frac{1}{N_{\mathbf{q}}} \sum_{\lambda} c_\lambda v_{\lambda,\alpha} v_{\lambda,\beta} \tau_\lambda^{\rm ph}. \tag{S1}$$

Here, α and β are indexing the Cartesian directions, $N_{\mathbf{q}}$ is the total number of $\mathbf{q}$-points sampled in the first Brillouin zone, while c_λ, v_λ and $\tau_\lambda^{\rm ph}$ denote the volumetric heat capacity, phonon group velocity, and phonon relaxation time, respectively. Note that $c_\lambda = (\hbar\omega_\lambda/V)(\partial n_\lambda^0/\partial T)$, where n_λ^0 is the Bose-Einstein distribution function and V the volume of the primitive cell, and $v_{\lambda,\alpha} = \partial\omega_\lambda/\partial q_\alpha$. Phonons can be scattered on other phonons, electrons, impurities, or grain boundaries. With the Matthiessen's rule [5], the phonon scattering rate ($\tau_\lambda^{\rm ph}$) is a summation of the phonon-phonon ($1/\tau_\lambda^{\text{ph-ph}}$), phonon-electron ($1/\tau_\lambda^{\text{ph-el}}$), phonon-impurity ($1/\tau_\lambda^{\text{ph-im}}$), phonon-isotope ($1/\tau_\lambda^{\text{ph-iso}}$), and phonon-grain boundary ($1/\tau_\lambda^{\text{ph-gb}}$) scattering rates. Here we predict the $\kappa_{\rm ph}$ of two-dimensional (2D) BeN_4 based on *ab initio* computed $1/\tau_\lambda^{\text{ph-ph}}$ with three-phonon (3ph), four-phonon (4ph), phonon-isotope, and phonon-electron (ph-el) scattering rates

$$\frac{1}{\tau_\lambda^{\rm ph}} = \frac{1}{\tau_\lambda^{\rm 3ph}} + \frac{1}{\tau_\lambda^{\rm 4ph}} + \frac{1}{\tau_\lambda^{\text{ph-iso}}} + \frac{1}{\tau_\lambda^{\text{ph-el}}}, \tag{S2}$$

3ph scattering rates: $1/\tau_\lambda^{\rm 3ph}$ can be obtained by Fermi's golden rule (FGR) [5, 6] as

$$\frac{1}{\tau_\lambda^{\rm 3ph}} = \sum_{\lambda_1\lambda_2} \left(\frac{1}{2}\Gamma_\lambda^{\lambda_1\lambda_2} + \Gamma_{\lambda\lambda_1}^{\lambda_2} \right), \tag{S3}$$

where $\Gamma_{\lambda\lambda_1}^{\lambda_2}$ and $\Gamma_\lambda^{\lambda_1\lambda_2}$ represent the absorption and emission scattering in three-phonon scattering processes rates and can be calculated as [5, 7, 8]

$$\Gamma_\lambda^{\lambda_1\lambda_2} = \frac{\pi\hbar}{4N}(1+n_{\lambda_1}^0+n_{\lambda_2}^0)\left|\Psi_-^{\rm (3ph)}\right|^2 \Delta_{\mathbf{k}}^{\mathbf{k}_1\mathbf{k}_2} \frac{\delta(\omega_\lambda-\omega_{\lambda_1}-\omega_{\lambda_2})}{\omega_\lambda\omega_{\lambda_1}\omega_{\lambda_2}}, \tag{S4}$$

$$\Gamma_{\lambda\lambda_1}^{\lambda_2} = \frac{\pi\hbar}{4N}(n_{\lambda_1}^0-n_{\lambda_2}^0)\left|\Psi_+^{\rm (3ph)}\right|^2 \Delta_{\mathbf{k}\mathbf{k}_1}^{\mathbf{k}_2} \frac{\delta(\omega_\lambda+\omega_{\lambda_1}-\omega_{\lambda_2})}{\omega_\lambda\omega_{\lambda_1}\omega_{\lambda_2}}, \tag{S5}$$

$$\Psi_\pm^{\rm (3ph)} = \sum_{b,l_1b_1,l_2b_2} \sum_{\alpha\alpha_1\alpha_2} \Phi_{0b,l_1b_1,l_2b_2}^{\alpha\alpha_1\alpha_2} \frac{e_{\alpha b}^{\lambda} e_{\alpha_1 b_1}^{\pm\lambda_1} e_{\alpha_2 b_2}^{-\lambda_2}}{\sqrt{\bar{m}_b\bar{m}_{b_1}\bar{m}_{b_2}}} e^{\pm i\mathbf{k}_1\mathbf{r}_{l_1}} e^{-i\mathbf{k}_2\mathbf{r}_{l_2}}. \tag{S6}$$

$\Delta_{\mathbf{k}}^{\mathbf{k}_1\mathbf{k}_2}$ and $\Delta_{\mathbf{k}\mathbf{k}_1}^{\mathbf{k}_2}$ account for the momentum selection rules (Fermi's golden rule, FGR) for the absorption process $\mathbf{k}=\mathbf{k}_1+\mathbf{k}_2+\mathbf{R}$ and the emission process $\mathbf{k}+\mathbf{k}_1=\mathbf{k}_2+\mathbf{R}$ respectively, with the reciprocal lattice vector $\mathbf{R}=\mathbf{0}$ representing Normal (N) processes and $\mathbf{R}\neq\mathbf{0}$ representing Umklapp (U) processes. N is the total number of $\mathbf{k}$-points or primitive cells, n^0 is the Bose-Einstein distribution for accounting the phonon occupation number, ω is the phonon frequency, and e is the phonon eigenvector. l, b, and α label the indexes of unit cells, basis atoms, and (x,y,z) directions, respectively. $\Phi^{\alpha\alpha_1\alpha_2}_{0b,l_1b_1,l_2b_2}$ is third-order interatomic force constants (3rd-IFCs).

4ph scattering rates: Similarly, $1/\tau_\lambda^{\text{4ph}}$ can be obtained as [5, 7, 8]

$$\gamma_\lambda^{\text{4ph}}=\frac{1}{\tau_\lambda^{\text{4ph}}}=\left(\frac{1}{6}\sum_{\lambda_1\lambda_2\lambda_3}\Gamma_\lambda^{\lambda_1\lambda_2\lambda_3}+\frac{1}{2}\sum_{\lambda_1\lambda_2\lambda_3}\Gamma_{\lambda\lambda_1}^{\lambda_2\lambda_3}+\frac{1}{2}\sum_{\lambda_1\lambda_2\lambda_3}\Gamma_{\lambda\lambda_1\lambda_2}^{\lambda_3}\right), \tag{S7}$$

where $\Gamma_\lambda^{\lambda_1\lambda_2\lambda_3}$, $\Gamma_{\lambda,\lambda_1}^{\lambda_2\lambda_3}$, and $\Gamma_{\lambda\lambda_1\lambda_2}^{\lambda_3}$ account for the absorption, redistribution, and emission scattering rates in four-phonon scattering processes and can be obtained as [5, 7, 8]

$$\Gamma_\lambda^{\lambda_1\lambda_2\lambda_3}=\frac{\pi\hbar}{4N}\frac{\hbar}{2N}\frac{n^0_{\lambda_1}n^0_{\lambda_2}n^0_{\lambda_3}}{n^0_\lambda}\left|\Psi^{(\text{4ph})}_{--}\right|^2\Delta_{\mathbf{k}}^{\mathbf{k}_1\mathbf{k}_2\mathbf{k}_3}\frac{\delta(\omega_\lambda-\omega_{\lambda_1}-\omega_{\lambda_2}-\omega_{\lambda_3})}{\omega_\lambda\omega_{\lambda_1}\omega_{\lambda_2}\omega_{\lambda_3}}, \tag{S8}$$

$$\Gamma_{\lambda\lambda_1}^{\lambda_2\lambda_3}=\frac{\pi\hbar}{4N}\frac{\hbar}{2N}\frac{(1+n^0_{\lambda_1})n^0_{\lambda_2}n^0_{\lambda_3}}{n^0_\lambda}\left|\Psi^{(\text{4ph})}_{+-}\right|^2\Delta_{\mathbf{k}\mathbf{k}_1}^{\mathbf{k}_2\mathbf{k}_3}\frac{\delta(\omega_\lambda+\omega_{\lambda_1}-\omega_{\lambda_2}-\omega_{\lambda_3})}{\omega_\lambda\omega_{\lambda_1}\omega_{\lambda_2}\omega_{\lambda_3}}, \tag{S9}$$

$$\Gamma_{\lambda\lambda_1\lambda_2}^{\lambda_3}=\frac{\pi\hbar}{4N}\frac{\hbar}{2N}\frac{(1+n^0_{\lambda_1})(1+n^0_{\lambda_2})n^0_{\lambda_3}}{n^0_\lambda}\left|\Psi^{(\text{4ph})}_{++}\right|^2\Delta_{\mathbf{k}\mathbf{k}_1\mathbf{k}_2}^{\mathbf{k}_3}\frac{\delta(\omega_\lambda+\omega_{\lambda_1}+\omega_{\lambda_2}-\omega_{\lambda_3})}{\omega_\lambda\omega_{\lambda_1}\omega_{\lambda_2}\omega_{\lambda_3}}, \tag{S10}$$

$$\Psi^{(\text{4ph})}_{\pm\pm}=\sum_{b,l_1b_1,l_2b_2,l_3b_3}\sum_{\alpha\alpha_1\alpha_2\alpha_3}\Phi^{\alpha\alpha_1\alpha_2\alpha_3}_{0b,l_1b_1,l_2b_2,l_3b_3}\frac{e^\lambda_{\alpha b}e^{\pm\lambda_1}_{\alpha_1b_1}e^{\pm\lambda_2}_{\alpha_2b_2}e^{-\lambda_3}_{\alpha_3b_3}}{\sqrt{\bar{m}_b\bar{m}_{b_1}\bar{m}_{b_2}\bar{m}_{b_3}}}e^{\pm i\mathbf{k_1}\cdot\mathbf{r}_{l_1}}e^{\pm i\mathbf{k_2}\cdot\mathbf{r}_{l_2}}e^{-i\mathbf{k_3}\cdot\mathbf{r}_{l_3}}, \tag{S11}$$

$\Delta_{\mathbf{k}}^{\mathbf{k_1}\mathbf{k_2}\mathbf{k_3}}$, $\Delta_{\mathbf{k}\mathbf{k}_1}^{\mathbf{k_2}\mathbf{k_3}}$, and $\Delta_{\mathbf{k}\mathbf{k}_1\mathbf{k_2}}^{\mathbf{k_3}}$ specify the momentum selection rules (Fermi's golden rule, FGR) for the absorption process $\mathbf{k}=\mathbf{k}_1+\mathbf{k}_2+\mathbf{k}_3+\mathbf{R}$, redistribution process $\mathbf{k}+\mathbf{k}_1=\mathbf{k}_2+\mathbf{k}_3+\mathbf{R}$, and emission process $\mathbf{k}+\mathbf{k}_1+\mathbf{k}_2=\mathbf{k}_3+\mathbf{R}$, respectively, with the reciprocal lattice vector $\mathbf{R}=\mathbf{0}$ representing Normal (N) processes and $\mathbf{R}\neq\mathbf{0}$ representing Umklapp (U) processes. $\Phi^{\alpha\alpha_1\alpha_2\alpha_3}_{0b,l_1b_1,l_2b_2,l_3b_3}$ is 4th-IFCs. In order to calculate the $1/\tau_\lambda^{\text{3ph}}$ and $1/\tau_\lambda^{\text{4ph}}$, the 2nd-, 3rd-, and 4th-IFCs need to be determined.

ph-iso scattering rates: $1/\tau_\lambda^{\text{ph-iso}}$ is considered by the natural isotopic atoms and can be estimated by Tamura theory [9]

$$\frac{1}{\tau_\lambda^{\text{ph-iso}}}=\frac{\pi}{2}\omega_\lambda^2\sum_{i\in\text{u.c.}}g_i\left|\mathbf{e}^*_{\lambda'}(i)\cdot\mathbf{e}_\lambda(i)\right|^2\delta(\omega_\lambda-\omega_{\lambda'}) \tag{S12}$$

where $\mathbf{e}_\lambda$ is the normalized eigenvector of phonon mode λ and the asterisk denotes the complex conjugate. The mass variance factor is expressed as $g_i=\sum if_i(j)[1-m_i(j)/\bar{m}_i]^2$,

where $f_i(j)$, $m_i(j)$, and $\bar{m}_i$ is the concentration, atomic mass of the jth substitution atom and average mass of the ith atom.

ph-el scattering rates: $1/\tau_\lambda^{\text{ph-el}}$ can be obtained from the imaginary part of phonon self-energy $\prod_\lambda$ by $1/\tau_\lambda^{\text{ph-el}} = 2\text{Im}(\prod_\lambda)/\hbar$. It can be expressed as [10]

$$\frac{1}{\tau_\lambda^{\text{ph-el}}} = \frac{2\pi}{\hbar}\sum_{\mathbf{k},i,j} \left|g^\lambda_{j\mathbf{k}+\mathbf{q},i\mathbf{k}}\right|^2 \left(f^0_{i\mathbf{k}} - f^0_{j\mathbf{k}+\mathbf{q}}\right) \times \delta\left(\epsilon_{i\mathbf{k}} - \epsilon_{j\mathbf{k}+\mathbf{q}} + \hbar\omega_\lambda\right), \tag{S13}$$

where g is the e-p interaction matrix element, f^0 is the Fermi-Dirac distribution function, $\mathbf{k}$ is the electron wave vector, i and j are electron band indices, ϵ is the electron energy, and ω is the phonon frequency. The e-p matrix element which describes an event where an electron at initial state $|i,\mathbf{k}\rangle$ is scattered to $|j,\mathbf{k}+\mathbf{q}\rangle$ by a phonon mode $\lambda = (\mathbf{q}, v)$, is defined as [10]

$$g^\lambda_{j\mathbf{k}+\mathbf{q},i\mathbf{k}} = \sqrt{\frac{\hbar}{2\omega_\lambda}} \left\langle \psi_{j\mathbf{k}+\mathbf{q}} \right| \partial U_\lambda \left| \psi_{i\mathbf{k}} \right\rangle, \tag{S14}$$

where ψ is the ground-state Bloch wave function and ∂U_λ denotes the first-order derivative of the Kohn-Sham potential with respect to the phonon displacement.

S1.2. Electron transport

Combining the BTE and Onsager relations [5], the electronic transport thermal conductivity can be obtained as

$$\sigma_{\alpha\beta} = -\frac{e^2 n_s}{V}\sum_{i\mathbf{k}} \frac{\partial f^0_{i\mathbf{k}}}{\partial \epsilon_{i\mathbf{k}}} v^\alpha_{i\mathbf{k}} v^\beta_{i\mathbf{k}} \tau^{\text{el-ph}}_{i\mathbf{k}}, \tag{S15}$$

$$[\sigma S]_{\alpha\beta} = -\frac{e n_s}{VT}\sum_{i\mathbf{k}} (\epsilon_{i\mathbf{k}} - \mu) \frac{\partial f^0_{i\mathbf{k}}}{\partial \epsilon_{i\mathbf{k}}} v^\alpha_{i\mathbf{k}} v^\beta_{i\mathbf{k}} \tau^{\text{el-ph}}_{i\mathbf{k}}, \tag{S16}$$

$$K_{\alpha\beta} = -\frac{n_s}{VT}\sum_{i\mathbf{k}} (\epsilon_{i\mathbf{k}} - \mu)^2 \frac{\partial f^0_{i\mathbf{k}}}{\partial \epsilon_{i\mathbf{k}}} v^\alpha_{i\mathbf{k}} v^\beta_{i\mathbf{k}} \tau^{\text{el-ph}}_{i\mathbf{k}}, \tag{S17}$$

where e is the elementary charge, n_s is the number of electrons per state, V is the volume of the unit cell, $f^0_{i\mathbf{k}}$ is the electron distribution function, $\mathbf{v}_{i\mathbf{k}} = \frac{1}{\hbar}\frac{\partial \epsilon_{i\mathbf{k}}}{\partial \mathbf{k}}$ is the electron velocity, α and β denotes the directional component. $\boldsymbol{\sigma}$, $\underline{\mathbf{S}}$ and $\underline{\mathbf{K}}$ are 3×3 tensors. $\boldsymbol{\sigma}$ is the electrical conductivity, $\underline{\mathbf{S}}$ is the Seebeck coefficient, and $\underline{\mathbf{K}}$ is related to the electron thermal conductivity $\boldsymbol{\kappa_e} = \underline{\mathbf{K}} - \underline{\mathbf{S}}\boldsymbol{\sigma}\underline{\mathbf{S}}T$, where T is the temperature. The summation in these three equations is over all the electrons enumerated using electronic wave vector $\mathbf{k}$ and band index i. μ is the chemical potential. The electron relaxation time, limited by electron-phonon

interaction scatterings, can be obtained as [5]

$$\frac{1}{\tau_{i\mathbf{k}}^{\text{el-ph}}} = \frac{2\pi}{\hbar}\sum_{j}\sum_{\lambda}\left|g^{\lambda}_{j\mathbf{k}+\mathbf{q},i\mathbf{k}}\right|^{2}\Big\{\left(n_{\lambda}+f^{0}_{j\mathbf{k}+\mathbf{q}}\right)\delta\left(\epsilon_{i\mathbf{k}}+\hbar\omega_{\lambda}-\epsilon_{j\mathbf{k}+\mathbf{q}}\right) + \left(n_{\lambda}+1-f^{0}_{j\mathbf{k}+\mathbf{q}}\right)\delta\left(\epsilon_{i\mathbf{k}}-\hbar\omega_{\lambda}-\epsilon_{j\mathbf{k}+\mathbf{q}}\right)\Big\}\left(1-\frac{v_{i\mathbf{k}}v_{j\mathbf{k}+\mathbf{q}}}{|v_{i\mathbf{k}}|\,|v_{j\mathbf{k}+\mathbf{q}}|}\right). \tag{S18}$$

S2. Computational details

For phonon-phonon scattering rate calculations, all the computations of IFCs based on density functional theory (DFT) in this work are performed by employing projector-augmented-wave [11] (PAW) method, as implemented in the Vienna ab initio simulation package (VASP) [12]. Perdew-Burke-Ernzerhof [13] (PBE) with the projector-augmented-wave method [11] is used for exchange and correlation functionals. There is 1 chemical unit of BeN_4 in the primitive unit cell for two-dimensional (2D) structure with 5 atoms, which will be used to build the supercell in the following IFCs calculations. The plane-wave energy is truncated with 800 eV, the converged threshold for energy and atomic forces are set to be 10^{-12} eV and 0.0001 eV/Å, respectively. The Brillouin zone was sampled with 18×18×1 in the optimization calculations. The optimized lattice constants of 2D BeN_4 are a=4.27 Å, b=3.66 Å, and γ=64.58°, which are being 0.2% smaller for a=4.28 Å [14], 0.3% smaller for b=3.67 Å [14], and 0.03% smaller for γ=64.58°[14] compared to experimental data [14]. To avoid the interactions between the layers and its mirror caused by the periodic boundary conditions, the 2D BeN_4 sheets are isolated from each other by 25 ÃĚ of vacuum spacing, which enables the convergence of κ_{p}. In 2nd-IFCs calculations, we employed DFTP calculations based on the supercell of $6 \times 6 \times 1$ for 2D BeN_4. The phonon dispersion relation was then extracted using Phonopy [15] which was interfaced to VASP [12]. In 3rd-IFCs calculations, we adopted the finite difference method as implemented thirdorder.py packaged in ShengBTE [16]. The supercell of $4 \times 4 \times 1$ was used, and the cutoff radius of interatomic interactions was set to be 12th nearest neighboring (12th-NN) for 2D BeN_4. After obtaining the 2nd- and 3th-IFCs, the three-phonon scattering rates were calculated using ShengBTE [16] and the integration of Brillouin zone sampling was converged with $\mathbf{q}$-points of 50×50×1. In 4th-IFCs calculations, we also employed the finite difference method by an in-house code [8, 17]. The supercell of $4 \times 4 \times 1$ was used, and the cutoff radius of inter-

atomic interactions was set to be 3th-NN for 2D BeN_4. After obtaining the 2nd-, 3rd- and 4th-IFCs, the four-phonon scattering rates were calculated using the in-house code [8, 17] and the integration of Brillouin zone sampling was converged with **q**-points of 50×50×1. The convergence of phonon thermal conductivity with respect to IFCs cutoffs and (q)-points sampled in Brillouin zone are carefully discussed in Sec. S3.

For electron-phonon scattering rate calculations, all the self-consistent DFT and density functional perturbation theory (DFPT) calculations are implemented in Quantum Espresso [18]. The norm-conserving pseudopotentials [19] are used. The exchange and correlation (XC) functional is treated by Generalized Gradient Approximation ([13], GGA) in our calculations. The plane-wave energy is truncated with 120 Ry, the converged threshold for energy and atomic forces are set to be 10^{-12} eV and 10^{-6} eV/Å, respectively. The electronic integration over the Brillouin zone is approximated by the Gaussian smearing of 0.01 Ry for the self-consistent calculations. The Brillouin zone was sampled with 18×18×1 in the optimization calculations. The optimized lattice constants of 2D BeN_4 are a=4.27 Å, b=3.66 Å, and γ=64.58°, which are being 0.2% smaller for a=4.28 Å [14], 0.3% smaller for b=3.67 Å [14], and 0.0% smaller for γ=64.58°[14] compared to experimental data [14]. To avoid the interactions between the layers and its mirror caused by the periodic boundary conditions, the 2D BeN_4 sheets are isolated from each other by 25 Å of vacuum spacing, which enables the convergence of κ_p. The phonon perturbation is firstly calculated using DFPT based on a supercell of 6×6×1 as implemented in Quantum Espresso [18] and then the el-ph scattering matrix element is calculated in Electron-Phonon Wannier (EPW) package [20, 21]. The el-ph scattering matrix element is initially obtained on coarse electron (**k**-points) and phonon (**q**-points) wave vector grids and then interpolated to denser **k** and **q** grids using the maximally localized Wannier function basis as implemented in EPW [20, 21]. The coarse **k**-points with 18×18×1 and **q**-points with 6×6×1 are used in the Wannier interpolations. The convergence of el-ph scattering rates with respect to denser mesh of wave vector are carefully discussed in Sec. S3. Finally, the finer **k**-points with 500×500×1 and **q**-points with 200×200×1 was used to compute the el-ph scattering rate contributing to electron transport, and finer **q**-points with 50×50×1 and **k**-points with 200×200×1 was used to compute the el-ph scattering rate contributing to phonon transport. On the other hand, in order to model the charge doping system, the Fermi surface is shifted toward to the unoccupied energy states from the charge neutral point [22, 23]. Importantly, an in-house modified EPW

code [1, 2, 24] is used to predict the electron-phonon coupling scattering rates in order to compute the huge dense **k**- and **q**-points more efficiently.

It should be noted that we performed non-spin calculations in both Quantum espresso and VASP. The differences in the relaxed lattice constants, phonon dispersion, and electronic band structures between Quantum espresso and VASP are less than 0.5%.

S3. Convergence studies and validations of parameters

S3.1. Convergence of IFCs cutoff in phonon thermal conductivity calculations

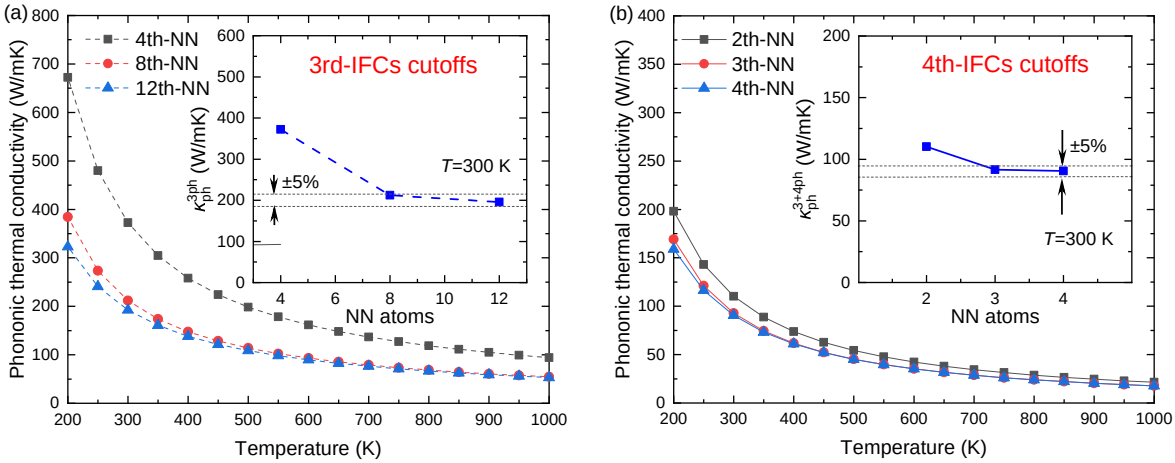

Fig. S1: $\kappa_{\rm ph}^{\rm 3ph}$ in (a) and $\kappa_{\rm ph}^{\rm 3+4ph}$ in (b) of 2D BeN_4 vary with temperature for different 3rd-IFCs and 4th-IFCs cutoffs, respectively. NN, 3ph, and 3+4ph denote nearest neighbors, 3ph scattering, and both 3ph and 4ph scatterings.

We plot $\kappa_{\rm ph}^{\rm 3ph}$ and $\kappa_{\rm ph}^{\rm 3+4ph}$ of 2D BeN_4 as a function of temperature for different IFCs cutoff as shown in Figs. **S1**(a) and (b), respectively. From Fig. **S1**(a), we can see that $\kappa_{\rm ph}^{\rm 3ph}$ changes within 3% in increasing the cutoff from 8th-NN to 12th-NN in 3ph scattering calculations. In 4ph scattering calculations, $\kappa_{\rm ph}^{\rm 3+4ph}$ changes within 5% in increasing the cutoff from 3rd-NN to 4th-NN shown in Fig. **S1**(b). Therefore, based on the trade-off between computational cost and accuracy, we finally include up to 12th-NN cutoffs in 3ph scattering calculations and 3th-NN in 4ph scattering calculations for 2D BeN_4, respectively.

S3.2. Convergence of q-points in phonon thermal conductivity calculations

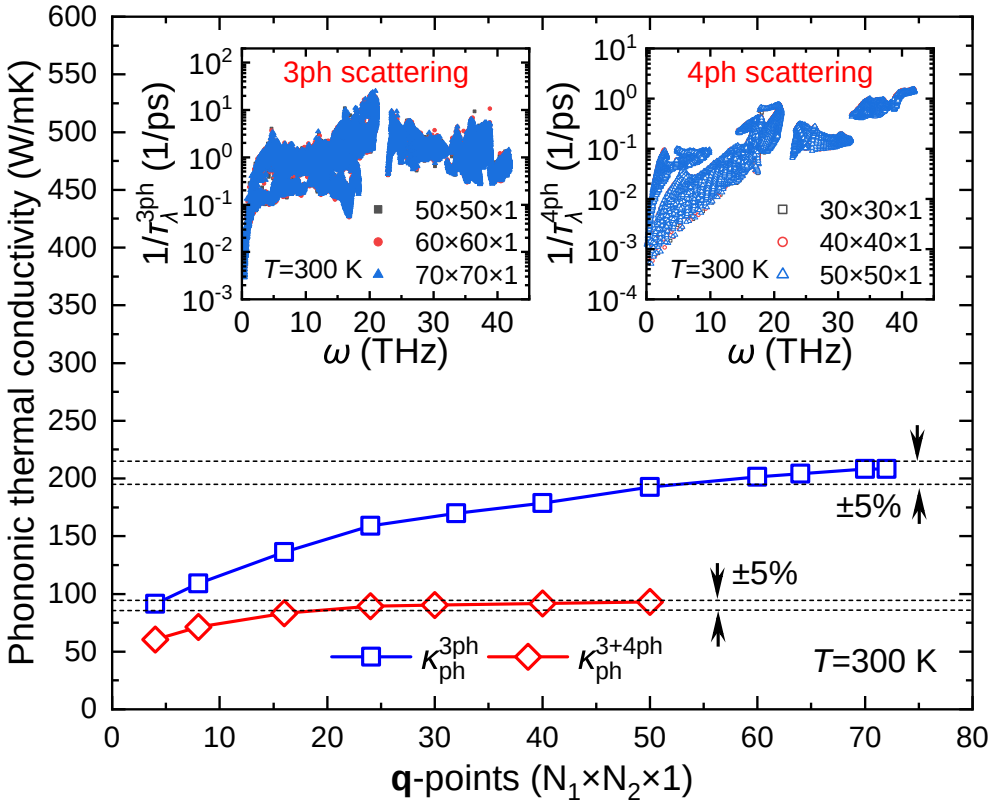

Fig. S2: Variation of $\kappa_{\rm ph}^{\rm 3ph}$ and $\kappa_{\rm ph}^{\rm 3+4ph}$ with **q**-points of 2D BeN_4.

The convergence of $\kappa_{\rm ph}^{\rm 3ph}$ and $\kappa_{\rm ph}^{\rm 3+4ph}$ with respect to Brillouin Zone sample density (**q**-points) is studied through calculating κ by considering different **q**-points density. Based on this, the $\kappa_{\rm ph}^{\rm 3ph}$ and $\kappa_{\rm ph}^{\rm 3+4ph}$ of 2D BeN_4 are plotted as a function of **q**-points as shown in Fig. **S2**. From the figure, we can see that $\kappa_{\rm ph}^{\rm 3ph}$ is converged to within 5% for an increase in **q**-points beyond $50 \times 50 \times 1$, while $\kappa_{\rm ph}^{\rm 3+4ph}$ is converged to within 3% for an increase in **q**-points beyond $40 \times 40 \times 1$. Therefore, in order to keep the balance of accuracy and computational cost, we finally use $50 \times 50 \times 1$ for both 3ph and 4ph scattering calculations.

S3.3. Validation of the Wannier interpolation

The Bloch electron states should be transformed to Wannier form to perform the interpolation [10] for calculating electron-phonon coupling matrix with dense **k**-points for electronic wave vector grid and **q**-points for phonon wave vector grid. *s* and *p* orbitals are included for both Be and N in the Wannier projections with 24 maximally localized Wannier functions (MLWFs) for interpolation. the coarse **k**-points with 18×18×1 and **q**-points with 6×6×1 are used in the Wannier interpolations. Figures **S3**(a) and (b) shows the electronic band

structure and phonon dispersions calculated by DFT and Wannier interpolation. The results match quite well with each other, indicating the reliability of Wannierization.

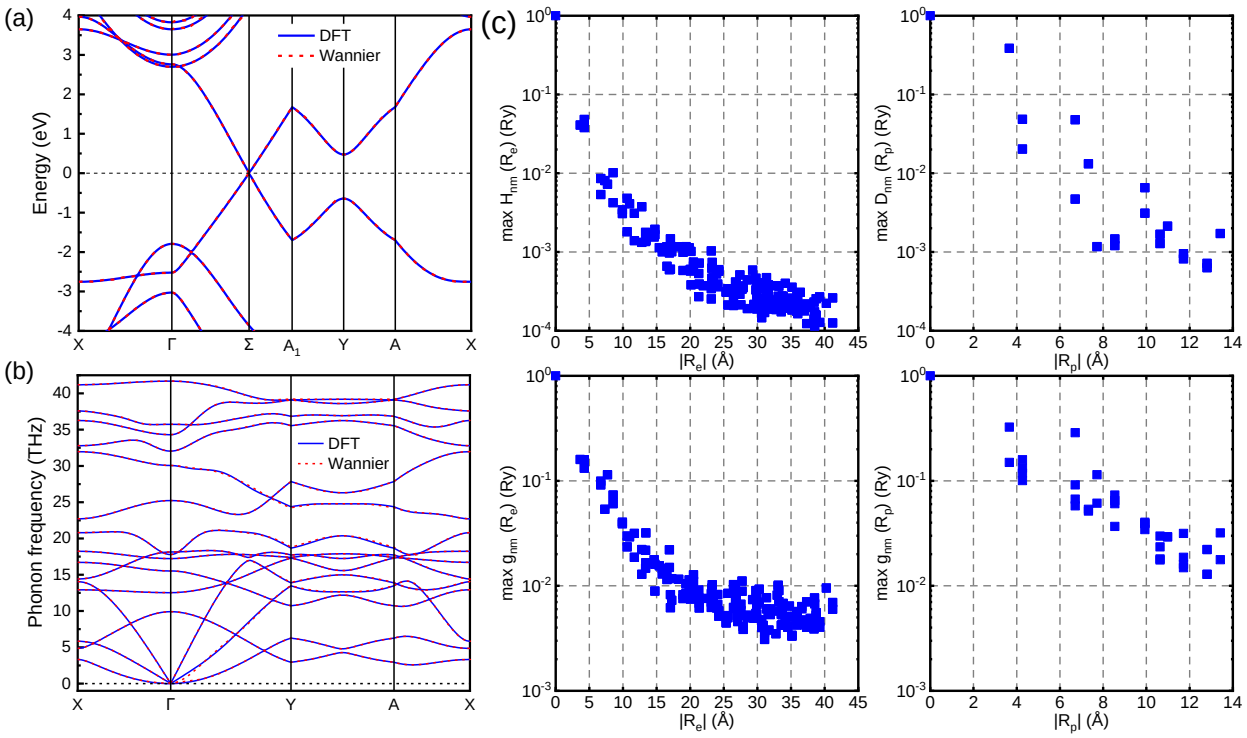

Fig. S3: (a) Electronic band structures of 2D BeN_4 calculated by DFT and Wannier interpolation technique. The electron energy is normalized to the Fermi energy. (b) Phonon dispersions of 2D BeN_4 calculated by DFT and Wannier interpolation technique. (c) Spatial decay of the largest component of the Hamiltonian, $\mathbf{H}(\mathbf{R}_e)$, dynamical matrix, $\mathbf{D}(\mathbf{R}_p)$, electron-phonon coupling matrix element, $g(\mathbf{R}_e)$, and $g(\mathbf{R}_p)$ for 2D BeN_4. The data are normalized against their largest values and are plotted as a function of position of the electron unit-cell, $\mathbf{R}_e$, or the phonon unit-cell, $\mathbf{R}_p$, used for describing electrons and phonons in the real space.

To further check the convergence of the coarse **k**-points and to get the converged coarse **q**-points, we plot the spatial decay of the Hamiltonian, the phonon dynamical matrix, and the electron-phonon coupling matrix elements in the Wannier functions representation for 2D BeN_4 in Fig. **S3**(c). All of these quantities should decay to zero in order to have the localized Wannier functions that are necessary for high-quality interpolation. As can be seen from Fig. **S3**(c), all of these quantities decay very quickly with distance, suggesting the sufficiency of the selected coarse **k**- and **q**-points for interpolation.

S3.4. Convergence of fine k- and q-points for electron-phonon coupling

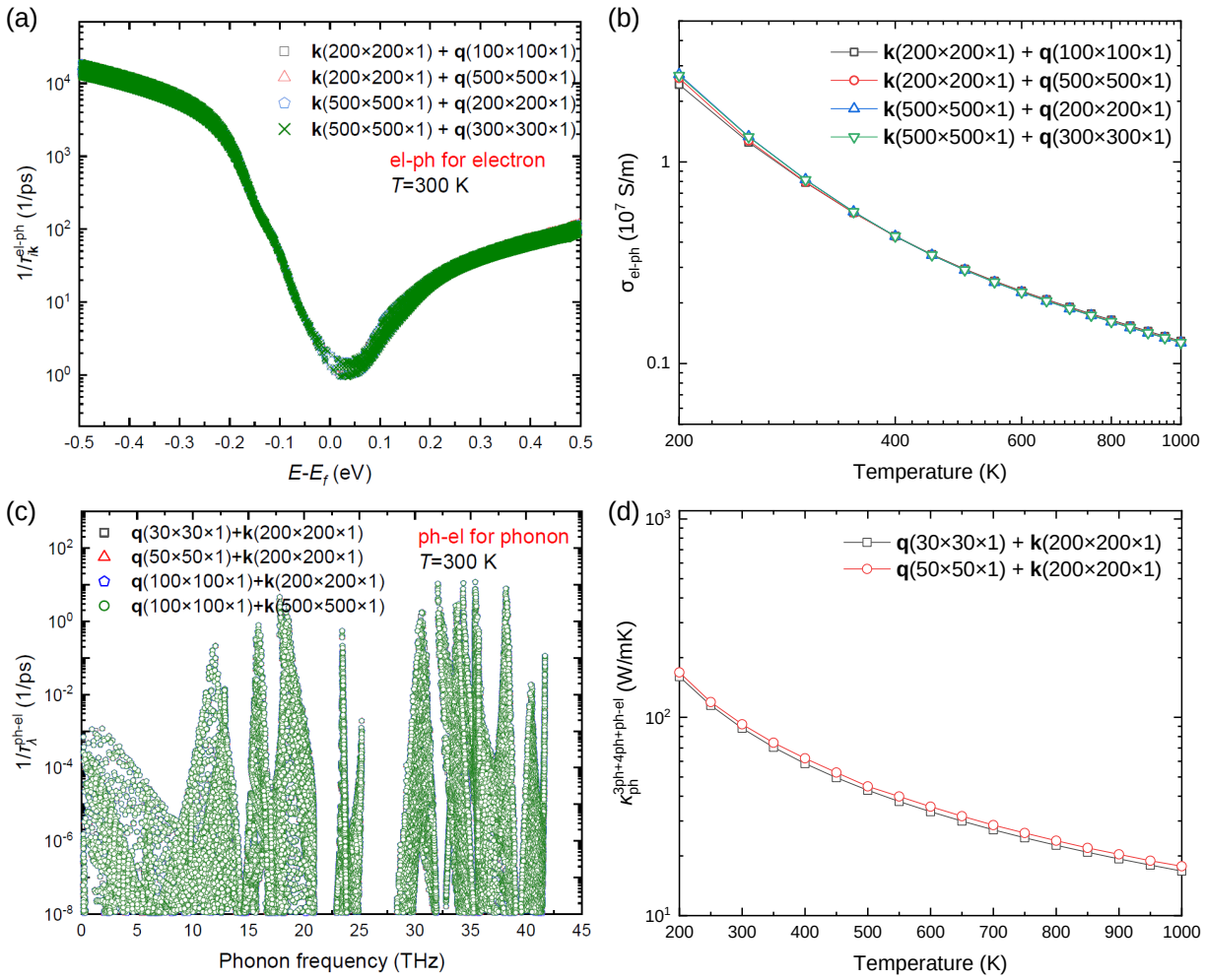

Fig. S4: (a) Variation of electron-phonon scattering rates ($1/\tau_{i\mathbf{k}}^{\text{el-ph}}$) contributing to electron thermal transport with fine **q**- and **k**-points at 300 K. (b) Variation of electrical conductivity ($\sigma_{\text{el-ph}}$) originating from electron-phonon scattering with fine **q**- and **k**-points. (c) Variation of phonon-electron scattering rates ($1/\tau_{\lambda}^{\text{ph-el}}$) contributing to phonon transport with fine **q**- and **k**-points at 300 K. (d) Variation of phonon thermal conductivity ($\kappa_{\text{ph}}^{\text{3ph+4ph+ph-el}}$) with fine **q**- and **k**-points.

The variations of the electron-phonon scattering rates contributing to phonon and electron transport of 2D BeN_4 with the fine **q**- and **k**-points are plotted in Fig. S4. As shown in Figs. S4(a) and (b), the electron-phonon scattering rates ($1/\tau_{i\mathbf{k}}^{\text{el-ph}}$) contributing to electron thermal transport and the electrical conductivity ($\sigma_{\text{el-ph}}$) originating from electron-phonon scattering are converged to within 2% for an increase in **k**-points beyond 200×200×1 and **q**-points beyond 200×200×1. To keep the balance between accuracy and computational cost, we finally used **k**-points with 500×500×1 and **q**-points with 200×200×1 for studying

electron transport properties due to electron-phonon coupling scatterings.

On other hand, as shown in Figs. S4(c) and (d), the electron-phonon scattering rates ($1/\tau_{\lambda}^{\text{ph-el}}$) contributing to phonon thermal transport and the phonon thermal conductivity ($\kappa_{\text{ph}}^{\text{3ph+4ph+ph-el}}$) are converged to within 2% for an increase in **k**-points beyond 200×200×1 and **q**-points beyond 50×50×1. It should be noted that in order to include the phonon-electron scattering into the computation of phonon thermal conductivity in which a consistent **q**-points is required in the implementation of computing 3ph, 4ph, and ph-el scattering rates, therefore we here only calculate the phonon thermal conductivity with **q**-points up to 50×50×1 shown in Fig. S4(d) due to the limitation of huge computation of 4ph scattering rates. Finally, to keep the balance between accuracy and computational cost, we used **q**-points with 50×50×1 and **k**-points with 200×200×1 for studying phonon transport properties due to electron-phonon coupling scatterings.

S3.5. Anisotropic thermal conductivity

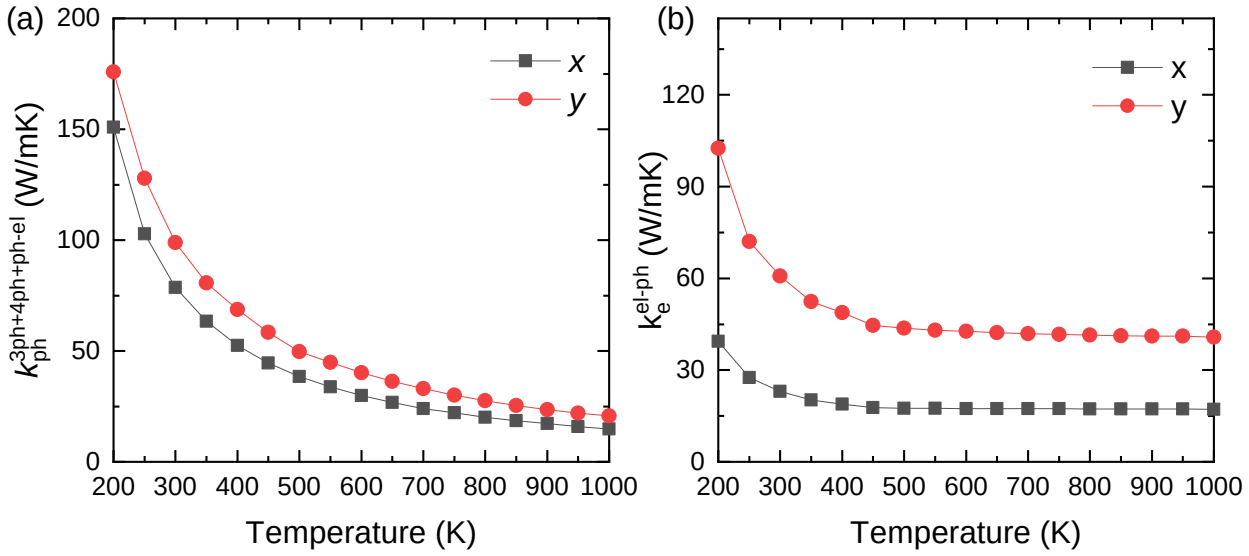

Fig. S5: Anisotropic thermal conductivity of (a) phonon $\kappa_{\text{ph}}^{\text{3ph+4ph+ph-el}}$ and (b) electron $\kappa_{\text{e}}^{\text{el-ph}}$ in intrinsic 2D BeN_4.

S4. Electrical resistivity of n-doped Graphene

In order to further validate our implementation of electron-phonon coupling calculations for predicting the electrical properties of doped material systems, here we first calculate the electrical resistivity of doped Graphene to validate our strategies which is adopted for 2D

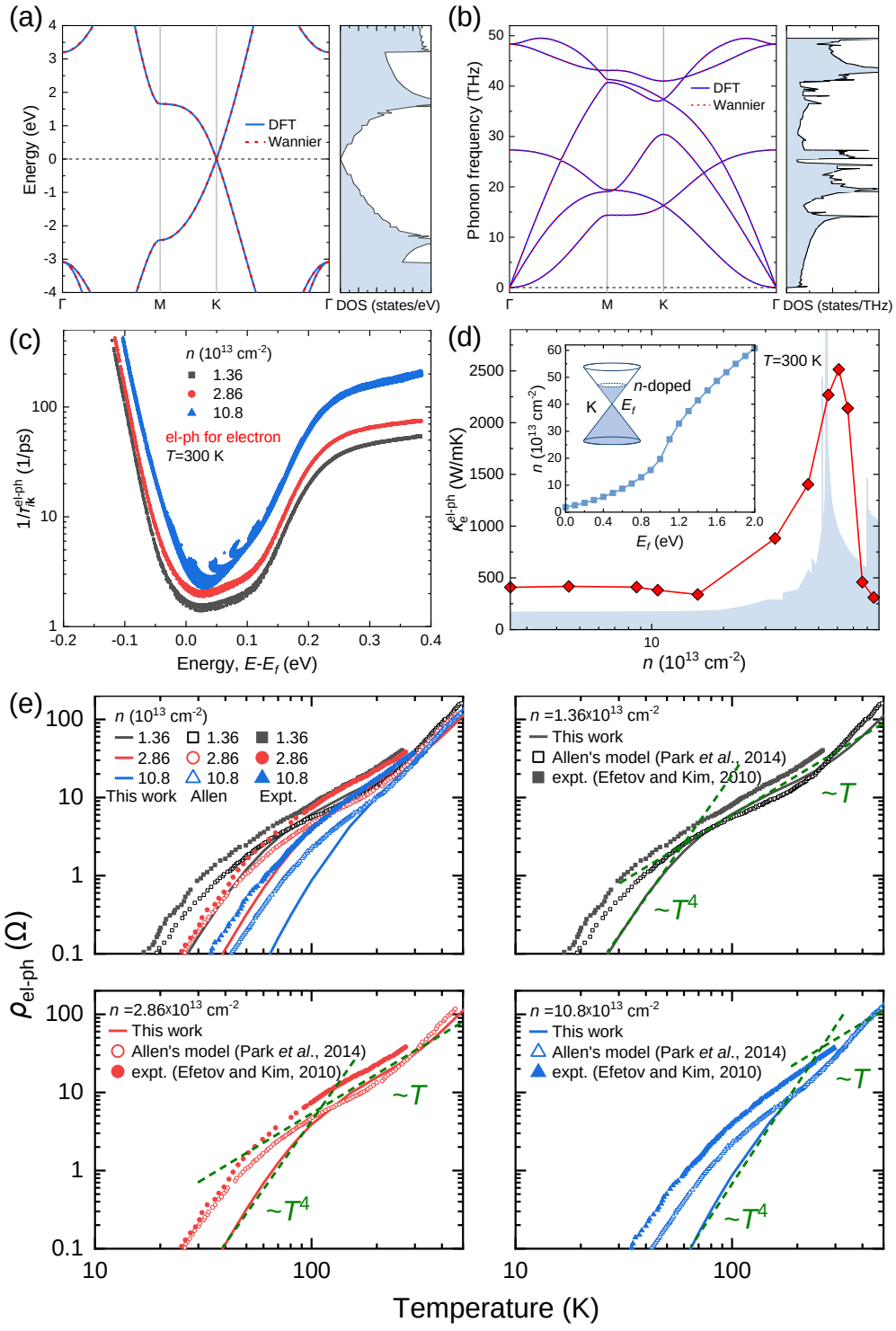

Fig. S6: (a) Electronic band structures of Graphene calculated by DFT and Wannier interpolation technique. The electron energy is normalized to the Fermi energy. (b) Phonon dispersions of Graphene calculated by DFT and Wannier interpolation technique. (c) Shifted Fermi level of doped Graphene. (d) Electron-phonon scattering of different doped carrier concentration with respect to Fermi level at 300 K. (e) Calculated electrical resistivity and reported data including DFT predictions [25] and experimental measurements [26] for Graphene with different doping concentration.

BeN_4 systems. The computational details for doped Graphene are as follows. By employing DFT and DFTP calculations, the energy of electrons and phonons are calculated with the Quantum-ESPRESSO package [18]. The norm-conserving pseudo-potential [19] is adopted and the local-density approximation (LDA)[27] is used for exchange and correlation. The kinetic energy cutoff of plane-wave basis is set as 60 Ry. The electronic integration over the Brillouin zone is approximated by the Gaussian smearing of 0.01 Ry for the self-consistent calculations. The Brillouin zone was sampled with 18×18×1 in the optimization calculations. To avoid the interactions between the layers and its mirror caused by the periodic boundary conditions, the graphene sheets are isolated from each other by 10 Å of vacuum spacing, which enables the convergence of κ_{p}. In order to model the charge doping system, the Fermi surface is shifted toward to the unoccupied energy states from the charge neutral point [22, 23]. The phonon perturbation is firstly calculated using DFPT based on a supercell of 8×8×1 as implemented in Quantum Espresso [18] and then the el-ph scattering matrix element is calculated in Electron-Phonon Wannier (EPW) package [20, 21]. The el-ph scattering matrix element is initially obtained on coarse electron (**k**-points) and phonon (**q**-points) wave vector grids with 8×8×1 and then interpolated to a convergence of el-ph scatterings with dense of 500×500×1 **k**-points and 200×200×1 **q**-points using the maximally localized Wannier function basis as implemented in our modified EPW package [1, 2, 24].

The calculated electron band structure, phonon dispersion, shifted Fermi level of doped Graphene, el-ph scattering rates, and electrical resistivity are shown in Fig. **S6**. Figure **S6**(e) compares our calculated electrical resistivity with reported data including DFT predictions [25] and experimental measurements [26] for different doping concentration of Graphene. We can see that our predictions overall agree well with the reported data especially for temperature higher than 200 K. The deviations at temperature lower then 200 K can be explained as following: (1) the experimental values [26] are higher then our predictions is attributed to the impurity or defects of the measuring samples which will induce extrinsic scatterings; (2) the DFT data from Park *et al.* [25] is calculated using Allen's [28] model and also include the electron-electron interactions which is important at low temperatures. Overall, our implementations give rise of very well agreement with reported data for temperature higher than 200 K, which demonstrates the reliability of our implementations for calculating the electron-phonon coupling transport properties of doped 2D BeN_4 in temperature range of 200 to 1000 K.

S5. Electron-phonon coupling strength

The mode-resolved electron-phonon coupling strength is defined as [21]

$$\lambda_{\rm tr}(\omega) = \frac{1}{N_F \omega_{\mathbf{q}\nu}} \sum_{i\mathbf{k}} \left| g^{\mathbf{q}\nu}_{j\mathbf{k}+\mathbf{q},i\mathbf{k}} \right|^2 \delta(\epsilon_{i\mathbf{k}} - \epsilon_F) \delta(\epsilon_{j\mathbf{k}+\mathbf{q}} - \epsilon_F) \left(1 - \frac{v_{i\mathbf{k}} v_{j\mathbf{k}+\mathbf{q}}}{|v_{i\mathbf{k}}|\,|v_{j\mathbf{k}+\mathbf{q}}|} \right), \tag{S19}$$

where N_F is the Fermi electron density-of -states per spin and per unit cell. The Eliashberg transport function $\alpha^2 F_{\rm tr}$ is further expressed as [21]

$$\alpha^2 F_{\rm tr}(\omega) = \frac{1}{2} \sum_{\mathbf{q}\nu} \omega_{\mathbf{q}\nu} \delta(\omega - \omega_{\mathbf{q}\nu}) \lambda_{\rm tr}(\omega_{\mathbf{q}\nu}). \tag{S20}$$

The $\alpha^2 F_{\rm tr}$ and $\lambda_{\rm tr}(\omega)$ of intrinsic and n-type beryllonitrene with $n = 13.8 \times 10^{14}$ cm^{-2} is shown in Fig. **S7**

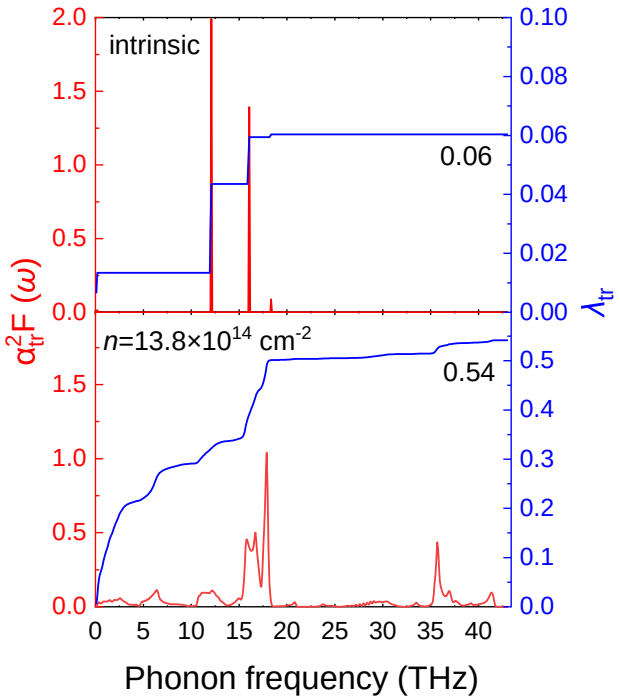

Fig. S7: Calculated transport Eliashberg spectral function $\alpha^2_{\rm tr}$F and transport electron-phonon coupling strength $\lambda_{\rm tr}$ of intrinsic and $n = 13.8 \times 10^{14}$ cm^{-2} at $T = 300$ K.

S6. Average electron relaxation time and group velocity

We predict the average electron relaxation time and group velocity using the following formulas

$$\langle \tau_{\rm e}^{\rm el\text{-}ph} \rangle = \frac{\sum_{i\mathbf{k}} (\epsilon_{i\mathbf{k}} - \epsilon_F)^2 \frac{\partial f^0_{i\mathbf{k}}}{\partial \epsilon_{i\mathbf{k}}} |v_{i\mathbf{k}}|^2 \tau^{\rm el\text{-}ph}_{i\mathbf{k}}}{\sum_{i\mathbf{k}} (\epsilon_{i\mathbf{k}} - \epsilon_F)^2 \frac{\partial f^0_{i\mathbf{k}}}{\partial \epsilon_{i\mathbf{k}}} |v_{i\mathbf{k}}|^2}. \tag{S21}$$

$$\langle v_{\rm e}\rangle = \sqrt{\frac{\sum_{i\mathbf{k}}(\epsilon_{i\mathbf{k}}-\epsilon_F)^2\frac{\partial f^0_{i\mathbf{k}}}{\partial\epsilon_{i\mathbf{k}}}|v_{i\mathbf{k}}|^2\tau^{\text{el-ph}}_{i\mathbf{k}}}{\sum_{i\mathbf{k}}(\epsilon_{i\mathbf{k}}-\epsilon_F)^2\frac{\partial f^0_{i\mathbf{k}}}{\partial\epsilon_{i\mathbf{k}}}\tau^{\text{el-ph}}_{i\mathbf{k}}}}. \tag{S22}$$

S7. Drude's free electron model for $\kappa_{\rm e}$

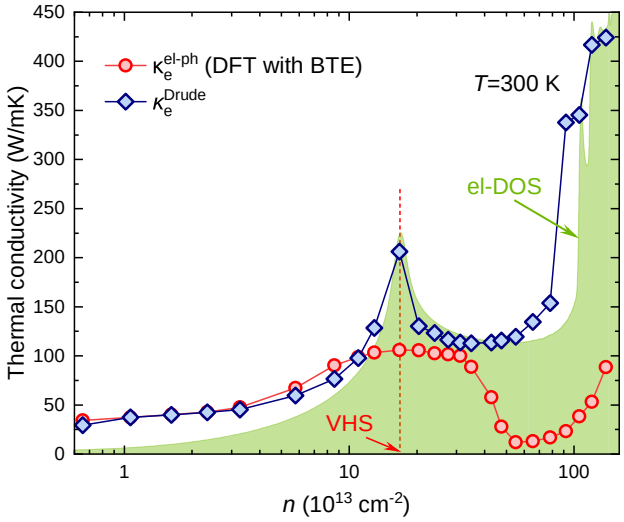

Fig. S8: Comparison of $\kappa_{\rm e}$ vs. n in beryllonitrene as obtained with a Drude's free electron model with $\tau = 12$ fs electron lifetime and with BTE and electron lifetime obtained from DFT.

S8. Allen's model for electron transport properties

According to Allen's model, the electrical resistivity is given by [28, 29]

$$\rho_{\text{el-ph}} = \frac{1}{\sigma_{\text{el-ph}}} = \frac{2\pi V k_B T}{e^2\hbar N_F\langle v_F^2\rangle}\int_0^\infty \frac{d\omega}{\omega}\frac{x^2}{\sinh^2 x}\alpha^2F_{\rm tr}(\omega), \tag{S23}$$

V is the volume of the unit cell, k_B^2 is the Boltzmann constant, T is the temperature, N_F is the Fermi electron density-of -states per spin and per unit cell, v_F^2 is the Fermi velocity, and ω is the frequency of phonon. $x = \hbar\omega/2k_B^2T$ is a dimensionless parameter. $\alpha^2F_{\rm tr}$ is the Eliashberg transport function defined in Eq. S20.

S9. Accumulation function of thermal conductivity

The phonon and electron thermal conductivity can be re-written as a function of phonon and electron mean free paths (MFP) with Λ_λ and $\Lambda_{i\mathbf{k}}$. These functions are called accumulation functions as expressed by [1, 2]

$$\kappa_{\mathrm{ph}}^{\alpha\beta}(\Lambda) = \sum_{\lambda}^{\Lambda_\lambda<\Lambda} c_\lambda \frac{v_{\lambda,\alpha} v_{\lambda,\beta}}{|\mathbf{v}_\lambda|} \Lambda_\lambda, \tag{S24}$$

$$\kappa_{\mathrm{e}}^{\alpha\beta}(\Lambda) = -\frac{n_s}{VT} \sum_{i\mathbf{k}}^{\Lambda_{i\mathbf{k}}<\Lambda} (\epsilon_{i\mathbf{k}} - \mu) \frac{\partial f_{i\mathbf{k}}^0}{\partial \epsilon} \frac{v_{i\mathbf{k},\alpha} v_{i\mathbf{k},\beta}}{|\mathbf{v}_{i\mathbf{k}}|} \Lambda_{i\mathbf{k}}, \tag{S25}$$

where $\Lambda_\lambda = |\mathbf{v}_\lambda|\,\tau_\lambda$ and $\Lambda_{i\mathbf{k}} = |\mathbf{v}_{i\mathbf{k}}|\,\tau_{i\mathbf{k}}$. The MFP is the definition of a distance between scattering events when a carrier travels.

* Electronic address: tongzhen@csar.ac.cn

† Electronic address: dtraian@umn.edu

‡ Electronic address: thomas.frauenheim@bccms.uni-bremen.de

[1] Z. Tong and H. Bao, International Journal of Heat and Mass Transfer **117**, 972 (2018).

[2] Z. Tong, S. Li, X. Ruan, and H. Bao, Physical Review B **100**, 144306 (2019).

[3] S. Li, A. Wang, Y. Hu, X. Gu, Z. Tong, and H. Bao, Materials Today Physics **15**, 100256 (2020).

[4] Z. Tong, T. Dumitrică, and T. Frauenheim, Nano Letters **21**, 4351 (2021).

[5] G. D. Mahan, Many-Particle Physics, 3rd ed. (Kluwer Academic/Plenum Publishers, New York, 2000).

[6] A. A. Maradudin and A. E. Fein, Physical Review **128**, 2589 (1962).

[7] L. Lindsay, D. A. Broido, and N. Mingo, Physical Review B **80**, 125407 (2009).

[8] T. Feng and X. Ruan, Physical Review B **93**, 045202 (2016).

[9] S.-i. Tamura, Physical Review B **27**, 858 (1983).

[10] F. Giustino, Reviews of Modern Physics **89**, 015003 (2017).

[11] G. Kresse and D. Joubert, Physical Review B **59**, 1758 (1999).

[12] G. Kresse and J. Hafner, Physical Review B **47**, 558 (1993).

[13] J. P. Perdew, K. Burke, and M. Ernzerhof, Physical Review Letters **77**, 3865 (1996).

[14] M. Bykov, T. Fedotenko, S. Chariton, D. Laniel, K. Glazyrin, M. Hanfland, J. Smith, V. Prakapenka, M. Mahmood, A. Goncharov, A. Ponomareva, F. TasnÃądi, A. Abrikosov, T. Bin Masood, I. Hotz, A. Rudenko, M. Katsnelson, N. Dubrovinskaia, L. Dubrovinsky, and I. Abrikosov, Physical Review Letters **126**, 175501 (2021).

[15] A. Togo and I. Tanaka, Scripta Materialia **108**, 1 (2015).

[16] W. Li, J. Carrete, N. A. Katcho, and N. Mingo, Computer Physics Communications **185**, 1747 (2014).

[17] Z. Tong, X. Yang, T. Feng, H. Bao, and X. Ruan, Physical Review B **101**, 125416 (2020).

[18] P. Giannozzi, S. Baroni, N. Bonini, M. Calandra, R. Car, C. Cavazzoni, D. Ceresoli, G. L. Chiarotti, M. Cococcioni, I. Dabo, A. Dal Corso, S. de Gironcoli, S. Fabris, G. Fratesi, R. Gebauer, U. Gerstmann, C. Gougoussis, A. Kokalj, M. Lazzeri, L. Martin-Samos, N. Marzari, F. Mauri, R. Mazzarello, S. Paolini, A. Pasquarello, L. Paulatto, C. Sbraccia, S. Scandolo, G. Sclauzero, A. P. Seitsonen, A. Smogunov, P. Umari, and R. M. Wentzcovitch, Journal of Physics: Condensed Matter **21**, 395502 (2009).

[19] N. Troullier and J. L. Martins, Physical Review B **43**, 1993 (1991).

[20] J. Noffsinger, F. Giustino, B. D. Malone, C.-H. Park, S. G. Louie, and M. L. Cohen, Computer Physics Communications **181**, 2140 (2010).

[21] S. Poncé, E. Margine, C. Verdi, and F. Giustino, Computer Physics Communications **209**, 116 (2016).

[22] S. Li, Z. Tong, and H. Bao, Journal of Applied Physics **126**, 025111 (2019).

[23] X. Yang, A. Jena, F. Meng, S. Wen, J. Ma, X. Li, and W. Li, Materials Today Physics **18**, 100315 (2021).

[24] S. Li, Z. Tong, X. Zhang, and H. Bao, Physical Review B **102**, 174306 (2020).

[25] C.-H. Park, N. Bonini, T. Sohier, G. Samsonidze, B. Kozinsky, M. Calandra, F. Mauri, and N. Marzari, Nano Letters **14**, 1113 (2014).

[26] D. K. Efetov and P. Kim, Physical Review Letters **105**, 256805 (2010).

[27] J. P. Perdew and Y. Wang, Physical Review B **45**, 13244 (1992).

[28] P. B. Allen, Physical Review B **17**, 3725 (1978).

[29] F. J. Pinski, P. B. Allen, and W. H. Butler, Physical Review B **23**, 5080 (1981).